REVIEW ARTICLE
PUBLISHED ONLINE: 24 AUGUST 2015 | DOI: 10.1038/NGEO2492
nature geoscience

Constraints from material properties on the dynamics and evolution of Earth's core

Christopher Davies[1,2]*, Monica Pozzo[3], David Gubbins[1,2] and Dario Alfè[3,4]

The Earth's magnetic field is powered by energy supplied by the slow cooling and freezing of the liquid iron core. Efforts to determine the thermal and chemical history of the core have been hindered by poor knowledge of the properties of liquid iron alloys at the extreme pressures and temperatures that exist in the core. This obstacle is now being overcome by high-pressure experiments and advanced mineral physics computations. Using these approaches, updated transport properties for Fe–Si–O mixtures have been determined at core conditions, including electrical and thermal conductivities that are higher than previous estimates by a factor of two to three. Models of core evolution with these high conductivities suggest that the core is cooling much faster than previously thought. This implies that the solid inner core formed relatively recently (around half a billion years ago), and that early core temperatures were high enough to cause partial melting of the lowermost mantle. Estimates of core–mantle boundary heat flow suggest that the uppermost core is thermally stratified at the present day.

Turbulent motions in Earth's liquid outer core, a mixture of iron alloyed with lighter elements, generate the geomagnetic field through a dynamo process that converts kinetic energy into magnetic energy. Palaeomagnetic observations show that the field has persisted for at least the past 3.5 billion years[1], which raises a fundamental question: how was the dynamo powered over this period? The standard model asserts that mantle convection cools the core by extracting heat across the core–mantle boundary (CMB); the resulting buoyancy forces drive vigorous convection that keeps the light element concentration almost uniform and the temperature close to adiabatic. Cooling leads to freezing of the liquid from the bottom up[2] because the melting curve $T_m(P)$ increases more rapidly with pressure P than the adiabat $T_a(P)$. As the solid inner core grows, latent heat is released and the light elements partition selectively into the outer core, reducing its density compared to pure iron[3] and providing a source of gravitational power[4]. Additional heating comes from the presence of any radiogenic elements.

In general, higher CMB heat flows lead to faster rates of cooling and inner core growth and provide more power for driving the dynamo (see Methods for mathematical details). Increasing the conductive heat loss, either through a larger thermal conductivity or temperature gradient, reduces the available power. Because all of the gravitational energy goes into generating magnetic field it makes the biggest contribution to determining the available dynamo power[5]. As well as the cooling rate, gravitational energy depends on the nature and mass concentration c of light elements and $\tau = dT_m/dP - \partial T_a/\partial P$, the difference between adiabatic and melting temperature gradients at the inner core boundary (ICB). Increasing c enhances the compositional density anomalies whereas reducing τ means that more inner core material freezes in unit time; for a given cooling rate both effects act to increase the gravitational energy.

Early models of core evolution used ideal solution theory to obtain c directly from density without needing to specify the species and represented τ in terms of one or more free parameters[6,7]. The numbers allowed an ancient inner core; the associated gravitational energy powered the geodynamo over most of Earth's history, negating any concerns over sustaining a dynamo powered by thermal convection alone. This scenario became untenable following an upward revision of T_a, which increased the adiabatic gradient and hence the heat Q_a conducted down the adiabat (see equations (1) and (2) below). The prevailing view was that the inner core must be a young feature of the planet, around 1 billion years old[8], and that thermal convection alone could power the dynamo before inner core formation[9]. However, thermal history models still produced a wide range of results, owing to different choices for material properties rather than theoretical formulations[9].

The technical challenge of estimating core properties arises from the extreme pressures (135–363 GPa) and temperatures (~5,000 K). This challenge is now being met by *ab initio* calculations and by diamond anvil cell and shock wave experiments where available. *Ab initio* calculations deliver all the geophysically relevant parameters at the full range of core (P, c, T) conditions; they are ground truthed from experiments, which are usually conducted in more restrictive (P, c, T) regimes. Diamond anvil cell experiments are normally available only up to upper core (P, T) conditions, whereas shock wave experiments follow an equation of state defined by the physical properties of the material (the Hugoniot) and are therefore not able to explore the full (P, T) space relevant to the core (preheating or precompressing allows some movement in (P, T) space, but not enough to cover all the relevant conditions). Examples of validations of *ab initio* calculations on pure iron include the equation of state of the hexagonal close-packed crystal up to core pressures, both at room temperature[10–14] and on the Hugoniot[15,16], the speed of sound of the liquid[16,17], the isentropic compressibility and thermal expansivity of the solid on the Hugoniot[15,16], the phonon dispersions (vibrational frequencies of waves in crystals as a function of the wavevector) of the body-centred cubic crystal at ambient conditions[14,18], the density of states of hexagonal close-packed iron up to 150 GPa (ref. 19), the iron melting curve[17,20], and the ambient conditions electrical resistivity[21,22].

The most difficult quantities to calculate at core conditions happen to be the most critical for core and geodynamo models: thermal and electrical conductivities. Results have only been

[1]School of Earth and Environment, University of Leeds, Leeds LS2 9JT, UK. [2]Institute of Geophysics and Planetary Physics, Scripps Institution of Oceanography, University of California San Diego, 9500 Gilman Drive, La Jolla, California 92093-0225, USA. [3]Department of Earth Sciences and Thomas Young Centre at UCL, UCL, Gower Street, London WC1E 6BT, UK. [4]Department of Physics and Astronomy and London Centre for Nanotechnology, UCL, Gower Street, London WC1E 6BT, UK. *e-mail: c.davies@leeds.ac.uk

Table 1 | Core material properties for pure iron and three Fe-O-Si mixtures.

Symbol	100%Fe	82%Fe-8%O-10%Si	79%Fe-13%O-8%Si	81%Fe-17%O-2%Si
$\Delta\rho$ (g cm^{-3})	0.24 (ref. 17)	0.6 (ref. 40)	0.8 (ref. 33)	1.0 (ref. 33)
c_O^S	-	0.0002 (ref. 14)	0.0004 (ref. 14)	0.0006 (ref. 80)
c_{Si}^S	-	0.0554 (ref. 14)	0.0430 (ref. 14)	0.0096 (ref. 80)
c_O^L	-	0.0256 (ref. 14)	0.0428 (ref. 14)	0.0559 (ref. 80)
c_{Si}^L	-	0.0560 (ref. 14)	0.0461 (ref. 14)	0.0115 (ref. 80)
C_P (J kg^{-1} K^{-1})	**715** (ref. 56)-800 (ref. 53)	-	-	-
γ	1.4 (ref. 55)-**1.5** (refs 17,56)	-	-	-
$\Delta S(r_i)$ (k_B)	1.05 (ref. 17)	-	-	-
$L(r_i)$ (MJ kg^{-1})	0.75	-	-	-
$T_m(r_i)$ (K)	6,350 (refs 17,20)	5,900	5,580	5,320
$(dT_m/dP)\|_{r_i}$ (K GPa^{-1})	9.01	9.0	9.0	9.0
$\alpha_T(r_i)$ ($\times10^{-5}$ K^{-1})	1.0 (refs 54,56)	-	-	-
$T_a(r_o)$ (K)	4,735 (refs 17,20)	4,290	4,100	3,910
$(\partial T_a/\partial P)\|_{r_i}$ (K GPa^{-1})	6.96	6.25	6.00	5.80
$(\partial T_a/\partial r)\|_{r_o}$ (K km^{-1})	−1.15	−1.03	−1.00	−0.96
σ ($\times10^6$ S m^{-1})	1.36 (ref. 25), 1.4 (ref. 23), 1.86 (ref. 26*)	1.12 (ref. 25)	1.11 (ref. 25)	1.18 (ref. 80)
k (W m^{-1} K^{-1})	159 (ref. 25), 150 (ref. 23), 170 (ref. 26)	107 (ref. 25)	99 (ref. 25)	101 (ref. 80)
D_O ($\times10^{-8}$ m^2 s^{-1}) (ref. 25)	-	1.31	1.30	-
D_{Si} ($\times10^{-8}$ m^2 s^{-1}) (ref. 25)	-	0.52	0.46	-
ν (m^2 s^{-1}) (ref. 25)	6.9	6.8	6.7	-
α_O^D ($\times10^{-12}$ kg m^{-3} s^{-1})	-	0.72	0.97	1.11
α_{Si}^D ($\times10^{-12}$ kg m^{-3} s^{-1})	-	1.19	1.10	40.6
		O	**Si**	
α_c (refs 46,49)	-	1.1	0.87	
$(\partial\mu/\partial c_X^L)\|_{P,T}$ (eV atom^{-1})	-	1.02×10^{10}	1.40×10^{10}	

Models are named after the molar concentrations of mixtures of Fe, O and Si corresponding to the given density jump. Quantities in the first section define the core chemistry model. Numbers in the second section determine the core temperature properties in the third section. The core temperature is assumed to follow an adiabat, denoted T_a, and the melting temperature of the core alloy is denoted T_m. CMB values for transport properties calculated along the corresponding adiabats are given in the fourth section. The CMB radius is denoted r_o = 3,480 km, the present-day ICB radius is r_i = 1,221 km and k_B is Boltzmann's constant. Where a range is given, numbers in bold are used in the core models. *This value was derived at a presumed CMB temperature of 3,750 K.

obtained recently[23–28], and turn out to be two to three times higher than conventional estimates[29,30] of thermal conductivity k = 28–46 W m^{-1} K^{-1} (called 'low conductivities' henceforth). Crucially these new values ('high conductivities') have been obtained in both experiments and *ab initio* calculations. A very recent study[31] on a perfect iron crystal at ICB conditions suggests that a new effect (electron–electron scattering) would reduce the electrical conductivity back to the old values that were estimated for the liquid[29]. The proposed importance of strong correlation effects seems at odds with previous work[32], so these results await both experimental and theoretical confirmation. Therefore we focus mainly on the high conductivity values, although the lower values are included for completeness.

Here we present a synthesis of core material properties. Parameter values are discussed, followed by their geophysical significance. A brief description of the *ab initio* methods is provided in Methods.

Material properties for Earth's core

The thermodynamic state of the core is determined by three intensive variables: Pressure P, mass concentration of species X, c_X, and temperature T. Pressure is very close to the enormous hydrostatic pressure, which is determined from seismology by integrating $dP/dr = -\rho g$ over radius r. Here ρ is density and g is gravity. Constraints on c_X and T are derived from the seismically determined ICB density jump, $\Delta\rho$.

Part of the observed density jump, $\Delta\rho_m$ = 0.24 g cm^{-3} (ref. 17), is due to the phase change at the ICB; the rest determines the excess concentration of light elements in the outer core, which in turn affects the melting temperature and influences almost all terms in the energy and entropy budgets. Normal mode eigenfrequencies give a consistent result of $\Delta\rho = 0.8 \pm 0.2$ g cm^{-3} (ref. 33) but have a low resolution of about 400 km. Body waves have a much better resolution of a few kilometres, but the estimates vary widely because PKiKP is a noisy phase[34–36]; they give an upper bound of 1.1 g cm^{-3} (ref. 36). There is also evidence for an anomalously dense layer in the lowermost 150 km of the outer core[37], which probably has a chemical origin[38]. Two explanations have been proposed: the layer could be a stable density-stratified zone of partial melt through which light elements pass by progressive melting and freezing[38], or parts of the inner core could be melting, releasing excess heavy liquid into the outer core[39]. In either case normal modes would measure the density difference between the inner core and main part of the outer core, whereas body waves would measure the smaller difference between the solid inner core and the heavy liquid in the anomalous layer. We believe the normal mode estimates are more likely to represent the true compositional difference between the outer and inner cores. We consider the three values $\Delta\rho$ = 0.6, 0.8 and 1.0 g cm^{-3}, spanning the range of published estimates. The 0.6 value corresponds to the Preliminary Reference Earth Model (PREM; ref. 40).

Table 1 summarizes our best estimates of core material properties for pure iron and the three values of $\Delta\rho$. Supplementary Table 1 is an extended version of Table 1 and Supplementary Tables 2–4 provide polynomial representations of depth-varying properties. Models are labelled by the corresponding core composition as described below. After composition we discuss thermal properties, followed by transport properties, which must be calculated for specific (P, c, T) conditions.

Composition. Composition is determined from the density (see Methods) and seismic velocities by comparing them with calculated values for mixtures of iron and candidate siderophile elements: Si and O, because of their abundance, and S, because of its presence in iron meteorites, which are thought to be remnants of planetary cores. Other elements, for example, H, have been proposed[41] but their properties in iron mixtures have not yet been explored extensively. The core also probably contains some Ni; however, recent experiments found that adding up to 10% of Ni does not change the hexagonal close-packed crystal structure of the solid[42], whereas *ab initio* calculations suggest that at high T the seismic properties of Fe–Ni alloys are almost indistinguishable from those of pure iron[43]. Recent studies of core composition[44–46] conclude that the light elements are likely to be Si, S and O, with negligible amounts of H and C. *Ab initio* calculations for Fe–S, Fe–Si and Fe–O mixtures show that S and Si partition almost equally between solid and liquid, whereas almost all the O goes into the liquid[14,45]. The behaviour of S and Si are very similar[14] so we use a Fe–Si–O mixture in this review. Mass concentrations of species X for the solid and liquid, c_X^S and c_X^L respectively, are given in top section of Table 1; each model is named after the corresponding molar concentration.

Temperature. Light element X depresses the melting temperature for pure iron, T_m, by an amount ΔT_X. Of particular importance are conditions near the ICB (radius $r = r_i$, $P = 330$ GPa). The large volume of work on T_m is summarized elsewhere[20,47]. Some studies have shown encouraging agreement, with $T_m(r_i) = 6{,}350 \pm 300$ K predicted by diamond anvil cell experiments up to 82 GPa (ref. 47) and 200 GPa (ref. 20), shock experiments at 225–260 GPa (ref. 48) and *ab initio* calculations at 330 GPa (refs 14,49). This value is used in second section of Table 1. Other calculations have found $T_m(r_i) = 7{,}100$ K (ref. 50) and $T_m(r_i) = 5{,}400$ K (ref. 51), but these only used *ab initio* indirectly by fitting an interatomic potential which has different melting properties from those of the fully *ab initio* system[52].

Along with $T_m(r_i)$ and the core chemistry model, the entropy of melting for pure iron ΔS is needed to determine ΔT_X at the ICB (ref. 49). The core temperature at the ICB, T_i, equals the melting temperature of the mixture; the values in second section of Table 1 are calculated from $T_i = T_m(r_i) + \Delta T_O + \Delta T_{Si}$. The latent heat L released on freezing the inner core is $L = T_m \Delta S$ (second section of Table 1).

In regions where convection is active the outer core temperature follows an adiabat, given by

$$T_a = T_i e^{\left(-\int_{r_i}^{r} (\rho g \gamma / K_S) dr\right)} \quad (1)$$

where γ is the thermodynamic Grüneisen parameter. Note that $\partial T_a/\partial r = -\rho g \gamma T_a/K_S$. The bulk modulus, K_S, and gravity, g, are calculated directly in *ab initio* methods and are very similar to PREM. *Ab initio* calculations have found that $\gamma \approx 1.5$ at the CMB and remains constant[17] (to within the accuracy of the calculations) or decreases slightly[53,54] with depth. The depth variation reduces $\partial T_a/\partial r$ and increases $\tau = dT_m/dP - \partial T_a/\partial P$, but the differences are minor. Depth variation of T_a is therefore well constrained. The three adiabats used in the core evolution calculations below are shown in Fig. 1; values for the CMB and ICB gradients are given in third section of Table 1. In the inner core, T_a was assumed to be close to isothermal[27].

The thermal and chemical expansion coefficients, $\alpha_T = -\rho^{-1}(\partial\rho/\partial T)_{P,c}$ and $\alpha_c = -\rho^{-1}(\partial\rho/\partial c)_{P,T}$, determine the buoyancy forces arising from thermal and compositional anomalies. α_T can be obtained from a number of thermodynamic relations, for example, $\alpha_T = \gamma\rho C_P/K_S$. *Ab initio* calculations have found the specific heat $C_P = 700 - 800$ J kg^{-1} K^{-1}, independent of radius[54], in agreement with theory[55], and hence α_T is a decreasing function of depth[55,56] because of the factor ρ/K_S. The compositional expansion coefficient α_c is different for each element; values obtained at present ICB (P, T) conditions[49] are given in Table 1.

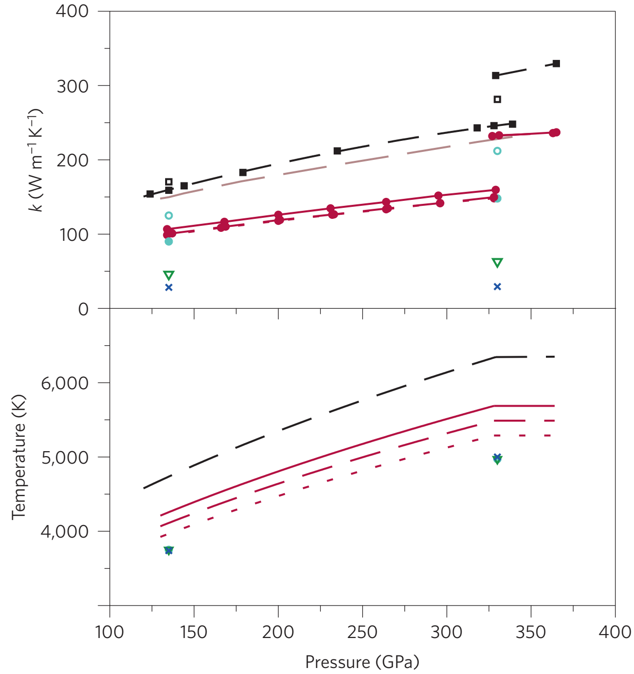

Figure 1 | Comparison of thermal conductivity estimates (top) and adiabatic temperature profiles (bottom) from different studies. The core chemistry models in Table 1 are shown in black (100%Fe; ref. 24) and red (82%Fe-8%O-10%Si, solid line[25]; 79%Fe-13%O-8%Si, long-dashed line[25]; 81%Fe-17%O-2%Si, short-dashed line[80]). Data from two other recent studies are shown for pure Fe (open black squares[26], brown dashed line[23] using the volume–temperature data of Pozzo *et al.*[24]), a mixture of 76.8%Fe-23.2%O (open aqua circles[26]) and a mixture of 77.5%Fe-22.5%Si (filled aqua circles[26]). Two older estimates of k are shown by the open green triangles[29] and blue crosses[30]. Inner core values were obtained from calculations on solid mixtures[27].

Transport properties. The geophysical importance of core thermal (k) and electrical (σ) conductivities is discussed below. σ is easier to obtain and is sometimes used to infer k through the Wiedemann–Franz law, although there are situations when this relation does not hold (see Methods). Recent estimates of k and σ for pure iron[23,24,26] are three to five times higher at the CMB than previous estimates[29,30] and increase by a factor of 1.5 to the ICB. Mixtures have also been studied, although using different compositions and adiabats. Despite this, and the different methods used, the studies all find k at the CMB in the range 80–110 W m^{-1} K^{-1}, increasing up to 140–160 W m^{-1} K^{-1} at the ICB (refs 23,25,26; Fig. 1). There is a jump in both k and σ at the ICB, and a small increase across the inner core[27].

Mass diffusion coefficients D_X relate the concentration gradient of species X to the diffusive flux of that species. Recent estimates[25,57] of D_O and D_{Si} agree with previous calculations at CMB pressures[58] and show a factor 1.5 increase to the ICB. In core evolution models D_X enters the barodiffusion term, which describes the entropy generated by diffusion of light elements down the ambient pressure gradient. The effect is measured by the barodiffusive coefficients α_X^D, which are calculated using the values of D_X and $(\partial\mu/\partial c_X^L)_{P,T}$ in Table 1, where μ is the chemical potential[58]. Barodiffusion is small enough to be neglected in the entropy budget[9,58,59], but might play

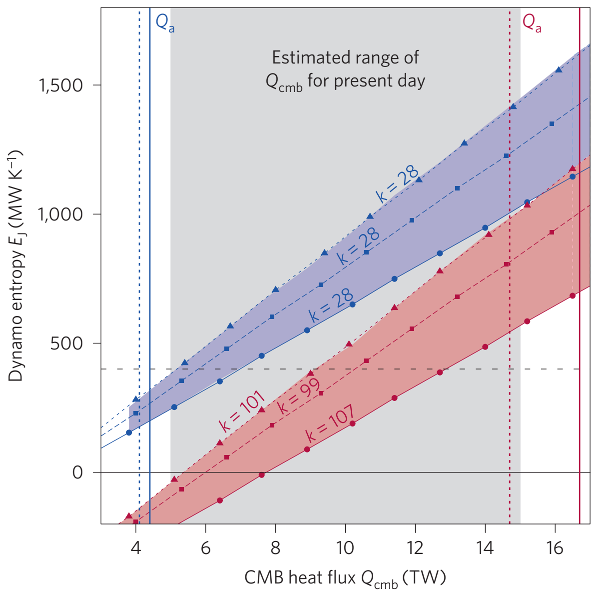

Figure 2 | Present-day core energy budget. Models with high values of the thermal conductivity k use the red profiles in Fig. 1 that have been calculated for $\Delta\rho = 0.6$ (solid lines), 0.8 (long-dashed lines) and 1.0 g cm^{-3} (short-dashed lines); models in blue use $k = 28$ W m^{-1} K^{-1} for each $\Delta\rho$. Other parameters are given in Table 1. Vertical lines indicate ranges for the heat Q_a lost down the core adiabat (colour and linetype again denote k and $\Delta\rho$ respectively). The horizontal black dashed line indicates a plausible estimate for E_J (ref. 65). Dynamo action requires $E_J > 0$. The grey shaded region indicates present-day estimates of CMB heat flow[62,63]. For $Q_{cmb} < Q_a$ any convection in the uppermost core is driven compositionally against thermal stratification.

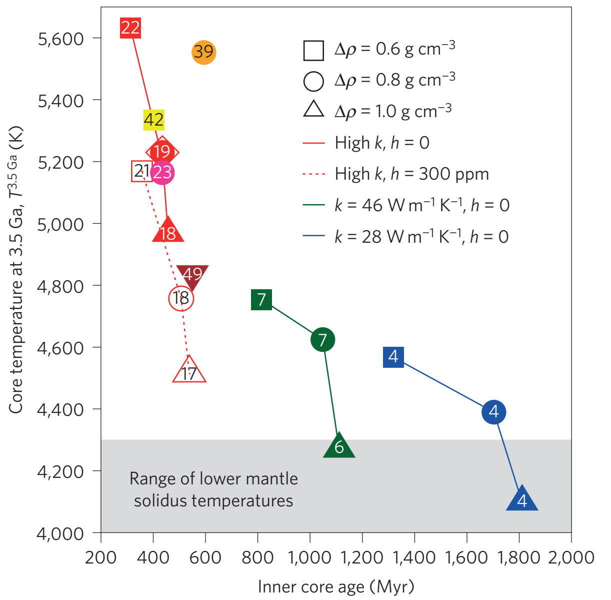

Figure 3 | Core thermal evolution. Numbers inside each symbol give CMB heat flow (in TW) at 3.5 Ga. High k models use the red profiles in Fig. 1 that have been calculated for each $\Delta\rho$; models in blue and green use the same k for each $\Delta\rho$. Models joined by lines use $E_J = 0$ before inner core formation, after which Q_{cmb} is set constant to ensure the outer core remains just superadiabatic. Results from other recent studies are shown in yellow[68], pink[63], orange[70] and maroon[69]. The inverted triangle denotes that $\Delta\rho$ did not enter into this formulation. Open diamond denotes the reference case in Fig. 4.

a dynamical role near the top of the core (see the 'stratification' subsection below).

The kinematic viscosity ν plays a key role in the dynamics of rotating fluids[60], but is less important for determining long-term core evolution. Recent *ab initio* estimates[25,57] of ν are given in Table 1 for the present core chemistry model; they are in line with older values[61].

Geophysical implications of revised core properties

Core energy budget. The dynamo entropy E_J represents the work done by buoyancy forces that goes into generating magnetic field[5] and is therefore crucial for assessing the viability of dynamo action. Both E_J and the CMB heat flow Q_{cmb} are related to the core cooling rate through the material properties described above: higher heat flow yields faster cooling and higher E_J (see Methods for details). The cooling rate determines the inner core age. Mantle convection sets the CMB heat flow and various lines of evidence suggest $Q_{cmb} = 5$–15 TW at present[62,63]. E_J could be calculated directly if we had detailed knowledge of the magnetic field throughout the core; however, the main field contributions to E_J occur at scales that cannot be observed[64] and so E_J is determined from Q_{cmb} for the present day. On longer timescales, where both Q_{cmb} and E_J are hard to estimate, the constraint $E_J \geq 0$ can be used to calculate lower bounds on the cooling rate. All parameter values are given in Table 1; the most important are $\Delta\rho$ and k, as we will show.

Increasing $\Delta\rho$ increases the outer core light-element concentration and reduces the adiabatic gradient (because $\partial T_a/\partial r$ is proportional to T_a), allowing the same E_J to be balanced with a lower cooling rate and hence lower Q_{cmb} (Fig. 2). For a plausible value[65] of $E_J = 400$ MW K^{-1}, increasing $\Delta\rho$ from 0.6 to 1.0 g cm^{-3} reduces the required CMB heat flow by 2 TW with low k and 4 TW with high k.

Increasing k increases the amount of heat conducted away down the adiabatic gradient, and hence reduces the dynamo efficiency (Fig. 2). The stability of core convection also depends critically on k. The total adiabatic heat flow is

$$Q_a = 4\pi r_o^2 k(r_o) \left.\frac{\partial T_a}{\partial r}\right|_{r=r_o} \tag{2}$$

When $Q_{cmb} > Q_a$ the whole core is superadiabatic and thermal convection occurs everywhere; when $Q_{cmb} < Q_a$ the top of the core is subadiabatic and stable to thermal convection. For a low value of $k = 28$ W m^{-1} K^{-1} the core is thermally unstable ($Q_{cmb} > Q_a$) and can generate a magnetic field ($E_J \geq 0$) for all estimates of present-day CMB heat flow (Fig. 2). For the high values of k dynamo action requires a minimum of 5.5–7.5 TW, whereas the top of the core is likely to be thermally stable unless $Q_{cmb} \approx 15$ TW. This is very high, around one-third of the total heat leaving Earth's surface[66]. Maintaining $E_J = 400$ MW K^{-1} with high values of k requires $Q_{cmb} = 9$–13 TW, with composition driving convection against thermal stratification in the uppermost core (Fig. 2).

Thermal history. To demonstrate the role of material properties in models of past core evolution we set $E_J = 0$ before inner core formation and specify Q_{cmb} during inner core growth. This prescription[9,59,63] ensures that $Q_{cmb} > Q_a$, consistent with the modelling assumptions (see Methods), and produces conservative estimates of the cooling rate, core temperature and inner core age. Figure 3 shows predicted inner core age and CMB temperature ($T^{3.5\,Ga}$) and CMB heat flow ($Q^{3.5\,Ga}$) at 3.5 Ga (Gyr ago), the time of the earliest palaeomagnetic measurement[1]. The influence of radiogenic heating is demonstrated by adding 300 ppm of ^{40}K at the present day, which probably represents an extreme scenario[44,63]. The shaded temperature range of 4,150 ± 150 K corresponds to present estimates of the lower mantle solidus temperature[67]; core temperatures exceeding this range suggest partial melting in the past.

Low-k models predict inner core ages of ~1 Gyr or more, CMB heat flows below 10 TW over the past 3.5 Gyr and ancient core temperatures at or above the lower mantle solidus estimates. With the high k values there is little doubt that the lowermost mantle would have been partially molten in the past. Moreover, the high-k models consistently yield inner core ages of 0.6 Gyr or younger. Radiogenic heating does little to change the results. Figure 3 also shows favoured models from four recent studies[63,68–70] that use the high k values and impose different constraints on the time variation of E_J. A consistent picture emerges: the inner core is at most 500–600 million years old; ancient core temperatures greatly exceeded present estimates of the lower mantle solidus; and high ancient CMB heat flows were needed to power the early geodynamo.

Increasing $\Delta\rho$ from 0.6 g cm^{-3} to 1.0 g cm^{-3} can produce a 400–600 K decrease in $T^{3.5\,\mathrm{Ga}}$ and a 200–400 Myr increase in the inner core age, depending on the details on the model (Fig. 3). Figure 4 shows how the results from a single reference case in Fig. 3 are influenced by individually varying values for several material properties compared to the numbers in Table 1. Where errors are not reported a ±10% variation is assumed, which is likely to be larger than errors in the *ab initio* calculations[17,56]. Individually changing α_c or L by ±10%, C_P to the values of a previous study[55], core density from PREM to AK135 (ref. 71), or the melting curve to a recent experimental profile[20] (denoted T_m^A) each make little difference. Using a depth variable γ (denoted γ^I; ref. 54) makes a small change to the inner core age but barely changes $T^{3.5\,\mathrm{Ga}}$. The biggest changes arise from varying k and allowing for the ±300 K uncertainty in T_i. Combining the variations to give the youngest (oldest) inner core yields changes of +(−)400 K in $T^{3.5\,\mathrm{Ga}}$ and −(+)150 Myr in inner core age compared to the reference model, which is a comparable effect to uncertainty in $\Delta\rho$ alone.

Stratification beneath the CMB. Observed variations in the magnetic field only reflect changes near the top of the core and so the dynamic stability of this region is an important issue. Stratified layers are dynamically very different from convecting regions: they suppress radial motion and support a different suite of waves[72]. In the absence of chemical or boundary effects, subadiabatic conditions at the top of the core (Fig. 2) should result in stable stratification. Compositional convection could overcome this stratification and mix the excess heat downwards, restoring adiabatic conditions everywhere[73]. Alternatively, light elements could enhance thermal stratification if they are emplaced at the top of the core early in Earth's history[74] or pool beneath the CMB over time. Pooling could arise from light element transfer across the CMB (ref. 75), by barodiffusion of light elements up the ambient pressure gradient[76], or by the transfer of chemically distinct blobs from the ICB (refs 74,77).

Kinematic models find that the stabilizing compositional gradient due to pooling overwhelms thermal effects, with layers of ~100 km depth[75,76] predicted even if the top of the core is thermally unstable. This is comparable to values inferred from geomagnetism[78], but thinner than recent seismic estimates[79]. In thermally stable and compositionally unstable conditions, establishing the net density stratification requires detailed analyses of the different buoyancy sources[26,70,80]. Two recent studies[78,80] find a thermochemically stable layer of ~100 km for a CMB heat flow of ~13 TW, compatible with current Q_{cmb} estimates[62]. Estimates of the associated density gradients from the recently proposed thermal/chemical stable layers yield Brunt frequencies of O(1) day[75,76,80], eliminating any longer-period vertical motion.

Density anomalies associated with core motions are so small that convection is unlikely to entrain or penetrate a stable layer[26,72,75,76]. The effect on a stable layer of thermal anomalies in the lowermost mantle is not so clear. The large-scale pattern of CMB heat flow can be constructed by assuming that observed

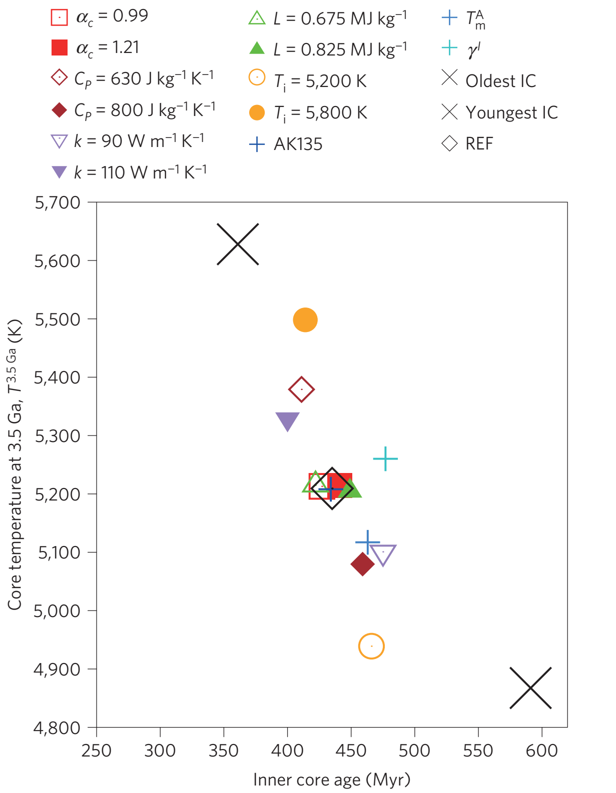

Figure 4 | Dependence of core thermal history predictions on various material properties. Each model uses identical parameters to the reference model, denoted REF and shown with a red open diamond in Fig. 3, except the quantity referred to in the legend. A ±10% variation in α_c, C_P and L from the values in Table 1 has been assumed. Values of k refer to the CMB and span the range in Table 1. Values of T_i span the ±300 K error estimates[14,20] described in the text. AK135 (ref. 71) is a model of core density. T_m^A is a recent experimentally determined melting curve[20]. Model γ^I uses a depth-dependent γ taken from a recent study[54]. The large crosses show the youngest and oldest inner core ages that can be achieved by combining the other variations.

seismic velocity variations represent thermal heterogeneity. The strength of the lateral variations is measured by the parameter $q^* = (q^{\max} - q^{\min})/(q_{\mathrm{cmb}} - q_a)$, the ratio of peak-to-peak boundary heat flow variations to the mean superadiabatic heat flow per unit area. Mantle convection simulations[81] have estimated $q^* \approx 2$, but apparently did not subtract the adiabat. The high values of k increase q_a, and hence q^*, further strengthening the effect.

Geodynamo simulations with $q^* \approx 1$ produce flows with persistent downwellings below regions of high CMB heat flow that concentrate magnetic flux there, producing field morphologies that are similar to the historical geomagnetic field[82,83]. These effects will be amplified when convection is weak at the top. Boundary-driven radial motions may generate flow in a stratified layer[80], as has been observed in non-magnetic simulations with weak stratification[84]. Geodynamo simulations that combine strong stratification and strong boundary anomalies ($q^* \gg 1$) are needed to establish whether the forcing can mix a statically stable layer.

The depth increase of k opens up the possibility that the very top of the core is superadiabatic, with a stable layer directly beneath[26,70]. The conditions required to form such a layer are sensitive to the $T_a(r)$ and $k(r)$ profiles; the models in this review do not produce such an effect.

Magnetic timescales. Revised core viscosity and diffusivities (Table 1) are too small to be used in present geodynamo simulations.

This situation is unlikely to change in the next ten years[60]. However, changes to the electrical conductivity σ are significant. The new (high) values of σ give a magnetic diffusivity of $\eta = 0.7\,\mathrm{m^2\,s^{-1}}$ at the CMB and $\eta = 0.6\,\mathrm{m^2\,s^{-1}}$ at the ICB, compared to $\eta = 1.6\,\mathrm{m^2\,s^{-1}}$ using a low value[29] of $\sigma = 5 \times 10^5\,\mathrm{S\,m^{-1}}$. Lowering η raises the magnetic Reynold's number $\mathrm{Rm} = (Ur_o)/\eta$ from ~700 to ~1,500, where U is the root mean square velocity at the top of the core[25,26]. Rm must be sufficiently large to generate a magnetic field by dynamo action. Decreasing η makes dynamo action possible with slower flows.

The time for a dipole magnetic field (the slowest decaying mode) to decay in a uniform sphere of radius r_o, the dipole decay time $\tau_d = r_o^2/\pi^2\eta$, is increased from 25 kyr to 55 kyr with the revised σ values. This result changes interpretations of all geomagnetic observations in terms of diffusion processes. In particular, polarity reversals of the field, which take 1–10 kyr to complete, now seem fast on the diffusion timescale. For the inner core $\tau_d = 10$ kyr, comparable to the timescale of reversal transition. Whether this is coincidence or a characteristic that distinguishes reversals from excursions[85] (where the new polarity is not retained) remains to be tested with modern geodynamo models.

Inner core convection. Seismic observations have revealed surprising structural complexity in the inner core, including hemispherical and radial variations in velocity and anisotropy[37]. Much recent work has focused on explaining these observations by solid-state convection[86]. Thermal convection requires the inner core to be superadiabatic; with the high values of $k \sim 200\,\mathrm{W\,m^{-1}\,K^{-1}}$ (Fig. 1) this requires $Q_{\mathrm{cmb}} = 30$–60 TW at the present day[27,87,88], at least two-thirds of the surface heat flow[66]. Just after inner core nucleation, 500–600 Myr ago (Fig. 3), an estimated 30 TW is needed[27]. Mantle heat sources are unlikely to have changed significantly in this period[89]; 30 TW probably represents at least half of Earth's total heat budget at this time.

Inner core convection could be driven compositionally if less light element partitions into it over time. Compositionally unstable conditions may have arisen once the inner core grew beyond O(10) km, but probably have not persisted to the present day[59,87]. The case of thermochemical buoyancy is complicated by possible double-diffusive effects; initial studies indicate that the net buoyancy force is stabilizing[90]. Overall it seems that inner core convection, either in the plume[86] or translation[39,91] regimes, is unlikely at present. This is consistent with a recent review that favours texturing mechanisms arising from magnetic coupling or heterogeneous growth due to enhanced equatorial heat loss[88]. If heterogeneous ICB heat flow is related to recent geomagnetic phenomena such as weak secular variation in the Pacific hemisphere[92] or long-term tilt of the dipole axis[93] then another mechanism (aside from convection) may be needed to explain the origin of the heat flow heterogeneity.

Core dynamics and evolution with high conductivities

The material properties of liquid iron alloys at high pressures and temperatures are now sufficiently constrained to draw robust conclusions about the long-term evolution of the core. Calculations employing the higher conductivity values find that: the inner core is less than 500 to 600 million years old[24,59,63,70]; the early core would have experienced high CMB heat flow, which implies core temperatures exceeding estimates of the lower mantle solidus temperature[59,63,68,94] and concomitant partial melting of the early Earth's lowermost mantle; and the present-day core is subadiabatic beneath the CMB and may be stably stratified[24,26,70]. In contrast, previous models (as illustrated in Figs 2 and 3) that employ lower conductivity values obtain an inner core age of at least one billion years[8], early core temperatures comparable to the lower mantle solidus[9], and superadiabatic conditions throughout the present-day core.

In terms of geophysical significance the most uncertain properties are the iron melting curve T_{m} and the ICB density jump $\Delta\rho$. However, the preceding conclusions will hold unless $\Delta\rho$ or T_{m} have been drastically underestimated. Core composition is also important: we have used an Fe–Si–O model, but other species such as H and C have been proposed. The effects of other putative light elements can be investigated routinely using *ab initio* methods and the results evaluated against geophysical constraints. The viability of a given composition can be assessed routinely in this manner. Finally, there is still some debate over the conductivity. The implications of old (low) conductivity values are shown in Figs 2 and 3. We favour the high values and discuss their implications below.

Revised core evolution models indicate that powering the dynamo around 3.5 Ga would have required a minimum Q_{cmb} of 15–25 TW to be extracted from the core by a partially molten lower mantle. The actual required Q_{cmb} at this time was probably much greater, partly because the core models assume a minimum dynamo entropy and partly because internal heat production within a magma ocean due to latent heat release and radiogenic sources would have insulated the core[95]. It has been proposed that the insulating effect was so drastic as to delay the onset of the core dynamo until about 2 Ga, with the magma ocean generating the field before this time[96]. Whether cooling alone is sufficient to power the early dynamo is at present an open question; indeed, the search for alternative energy sources has already begun[97].

Constraints on the core's material properties suggest that the uppermost core is subadiabatic unless Q_{cmb} has been underestimated. However, this seems unlikely, on the basis of the power requirements for mantle convection[62]. The magnetic field is generated by vigorous convection deep within the core, powered by latent heat release and gravitational energy. If light elements pool at the CMB, the top of the core will be stably stratified. Lateral variations in CMB heat flow are superimposed on the stratified layer. Geomagnetic data are at present unable to unambiguously identify a stable layer[98,99], although a recent constraint on core electrical conductivity from long-term dipole field variations is consistent with the high-conductivity estimates that argue in favour of stratification[100]. In isolation, both a stable layer and lateral heat flow variations can explain prominent features of the present geomagnetic field. Wave motions in an approximately 100-km-thick stable layer can account for short-period fluctuations in the dipole field[78] and regions of high CMB heat flow can concentrate magnetic field lines, producing the four dominant high-latitude flux patches[82]. In addition, low heat flow beneath the Pacific can explain the weak secular variation there[84].

Progress towards a coherent dynamical model of the present-day core requires improved seismic constraints on the strength and thickness of the stable layer beneath the CMB, a consistent model of recent geomagnetic secular variation in terms of stable layer dynamics, and analysis of the interaction between a stable region and CMB heat flow variations. The origin of a stable layer poses yet more fascinating challenges for future research.

Received 6 November 2014; accepted 25 June 2015; published online 24 August 2015

References

1. Tarduno, J. *et al.* Geodynamo, solar wind, and magnetopause 3.4 to 3.45 billion years ago. *Science* **327,** 1238–1240 (2010).
2. Jacobs, J. The Earth's inner core. *Nature* **172,** 297–300 (1953).
3. Birch, F. Elasticity and the constitution of Earth's interior. *J. Geophys. Res.* **66,** 227–286 (1952).
4. Braginsky, S. Structure of the F layer and reasons for convection in the Earth's core. *Sov. Phys. Dokl.* **149,** 8–10 (1963).
5. Lister, J. & Buffett, B. The strength and efficiency of thermal and compositional convection in the geodynamo. *Phys. Earth Planet. Inter.* **91,** 17–30 (1995).

6. Stevenson, D., Spohn, T. & Schubert, G. Magnetism and thermal evolution of the terrestrial planets. *Icarus* **54,** 466–489 (1983).
7. Mollett, S. Thermal and magnetic constraints on the cooling of the Earth. *Geophys. J. R. Astron. Soc.* **76,** 653–666 (1984).
8. Labrosse, S., Poirier, J.-P. & Le Moeul, J.-L. The age of the inner core. *Earth Planet. Sci. Lett.* **190,** 111–123 (2001).
9. Nimmo, F. in *Treatise on Geophysics* Vol. 9 (ed. Schubert, G.) 217–241 (Elsevier, 2007).
10. Söderlind, P., Moriarty, J. A. & Wills, J. M. First-principles theory of iron up to Earth-core pressures: Structural, vibrational, and elastic properties. *Phys. Rev. B* **53,** 14063 (1996).
11. Vočadlo, L., de Wijs, G. A., Kresse, G., Gillan, M. & Price, G. D. First principles calculations on crystalline and liquid iron at Earth's core conditions. *Faraday Discuss.* **106,** 205–218 (1997).
12. Mao, K., Wu, Y., Chen, L. C., Shu, J. F. & Jephcoat, A. P. Static compression of iron to 300 GPa and $Fe_{0.8}Ni_{0.2}$ alloy to 260 GPa: Implications for the composition of the core. *J. Geophys. Res.* **95,** 21737–21742 (1990).
13. Dewaele, A. *et al.* Quasihydrostatic equation of state of iron above 2 Mbar. *Phys. Rev. Lett.* **97,** 215504 (2006).
14. Alfè, D., Gillan, M. & Price, G. Temperature and composition of the Earth's core. *Contemp. Phys.* **48,** 63–80 (2007).
15. Alfè, D., Price, G. & Gillan, M. Thermodynamics of hexagonal close packed iron under Earth's core conditions. *Phys. Rev. B* **64,** 045123 (2001).
16. Brown, J. M. & McQueen, R. G. Phase transitions, Grüneisen parameter, and elasticity for shocked iron between 77 GPa and 400 GPa. *J. Geophys. Res.* **91,** 7485–7494 (1986).
17. Alfè, D., Price, G. & Gillan, M. Iron under Earth's core conditions: Liquid-state thermodynamics and high-pressure melting curve from *ab initio* calculations. *Phys. Rev. B* **65,** 165118 (2002).
18. Brockhouse, B. N., Abou-Helal, H. E. & Hallman, E. D. Lattice vibrations in iron at 296 K. *Solid State Commun.* **5,** 211–216 (1967).
19. Mao, H. K. *et al.* Phonon density of states of iron up to 153 gigapascals. *Science* **292,** 914–916 (2001).
20. Anzellini, S., Dewaele, A., Mezouar, M., Loubeyre, P. & Morard, G. Melting of iron at Earth's inner core boundary based on fast X-ray diffraction. *Science* **340,** 464–466 (2013).
21. Alfè, D., Pozzo, M. & Desjarlais, M. Lattice electrical resistivity of magnetic bcc iron from first-principles calculations. *Phys. Rev. B* **85,** 024102 (2012).
22. Weiss, R. J. & Marotta, A. S. Spin-dependence of the resistivity of magnetic metals. *J. Phys. Chem. Solids* **9,** 302–308 (1959).
23. de Koker, N., Steinle-Neumann, G. & Vlček, V. Electrical resistivity and thermal conductivity of liquid Fe alloys at high P and T and heat flux in Earth's core. *Proc. Natl Acad. Sci. USA* **109,** 4070–4073 (2012).
24. Pozzo, M., Davies, C., Gubbins, D. & Alfè, D. Thermal and electrical conductivity of iron at Earth's core conditions. *Nature* **485,** 355–358 (2012).
25. Pozzo, M., Davies, C., Gubbins, D. & Alfè, D. Transport properties for liquid silicon–oxygen–iron mixtures at Earth's core conditions. *Phys. Rev. B* **87,** 014110 (2013).
26. Gomi, H. *et al.* The high conductivity of iron and thermal evolution of the Earth's core. *Phys. Earth Planet. Inter.* **224,** 88–103 (2013).
27. Pozzo, M., Davies, C., Gubbins, D. & Alfè, D. Thermal and electrical conductivity of solid iron and iron–silicon mixtures at Earth's core conditions. *Earth Planet. Sci. Lett.* **393,** 159–164 (2014).
28. Ohta, K. Measurements of electrical and thermal conductivity of iron under Earth's core conditions *AGU* (Fall Meeting 2014) abstr. #MR21B-06 (2014).
29. Stacey, F. & Anderson, O. Electrical and thermal conductivities of Fe–Ni–Si alloy under core conditions. *Phys. Earth Planet. Inter.* **124,** 153–162 (2001).
30. Stacey, F. & Loper, D. A revised estimate of the conductivity of iron alloy at high pressure and implications for the core energy balance. *Phys. Earth Planet. Inter.* **161,** 13–18 (2007).
31. Zhang, P., Cohen, R. & Haule, K. Effects of electron correlations on transport properties of iron at Earth's core conditions. *Nature* **517,** 605–607 (2015).
32. Pourovskii, L., Mravlje, J., Ferrero, M., Parcollet, O. & Abrikosov, I. Impact of electronic correlations on the equation of state and transport in ε-Fe. *Phys. Rev. B* **90,** 155120 (2014).
33. Masters, G. & Gubbins, D. On the resolution of density within the Earth. *Phys. Earth Planet. Inter.* **140,** 159–167 (2003).
34. Cao, A. M. & Romanowicz, B. Constraints on density and shear velocity contrasts at the inner core boundary. *Geophys. J. Int.* **157,** 1146–1151 (2004).
35. Koper, K. D. & Dombrovskaya, M. Seismic properties of the inner core boundary from PKiKP/P amplitude ratios. *Earth Planet. Sci. Lett.* **237,** 680–694 (2005).
36. Tkalčić, H., Kennett, B. & Cormier, V. On the inner–outer core density contrast from PKiKP/PcP amplitude ratios and uncertainties caused by seismic noise. *Geophys. J. Int.* **179,** 425–443 (2009).
37. Souriau, A. in *Treatise on Geophysics* Vol. 1 (eds Schubert, G., Romanowicz, B. & Dziewonski, A.) Ch. 19, 655–693 (Elsevier, 2007).
38. Gubbins, D., Masters, G. & Nimmo, F. A thermochemical boundary layer at the base of Earth's outer core and independent estimate of core heat flux. *Geophys. J. Int.* **174,** 1007–1018 (2008).
39. Alboussière, T., Deguen, R. & Melzani, M. Melting-induced stratification above the Earth's inner core due to convective translation. *Nature* **466,** 744–747 (2010).
40. Dziewonski, A. & Anderson, D. Preliminary reference Earth model. *Phys. Earth Planet. Inter.* **25,** 297–356 (1981).
41. Nomura, R. *et al.* Low core–mantle boundary temperature inferred from the solidus of pyrolite. *Science* **343,** 522–524 (2014).
42. Tateno, S., Hirose, K., Komabayashi, T., Ozawa, H. & Ohishi, Y. The structure of Fe–Ni alloy in Earth's inner core. *Geophys. Res. Lett.* **39,** L12305 (2012).
43. Martorell, B., Brodholt, J., Wood, I. G. & Vocadlo, L. The effect of nickel on the properties of iron at the conditions of the Earth's inner core: *Ab initio* calculations of seismic wave velocities of Fe–Ni alloys. *Earth Planet. Sci. Lett.* **365,** 143–151 (2013).
44. Hirose, K., Labrosse, S. & Hernlund, J. Compositional state of Earth's core. *Annu. Rev. Earth Planet. Sci.* **41,** 657–691 (2013).
45. Morard, G., Andrault, D., Antonangeli, D. & Bouchet, J. Properties of iron alloys under the Earth's core conditions. *C. R. Geosci.* **346,** 130–139 (2014).
46. Badro, J., Côté, A. & Brodholt, J. A seismologically consistent compositional model of Earth's core. *Proc. Natl Acad. Sci. USA* **111,** 7542–7545 (2014).
47. Jackson, J. *et al.* Melting of compressed iron by monitoring atomic dynamics. *Earth Planet. Sci. Lett.* **362,** 143–150 (2013).
48. Nguyen, J. & Holmes, N. Melting of iron at the physical conditions of the Earth's core. *Nature* **427,** 339–342 (2004).
49. Alfè, D., Gillan, M. & Price, G. *Ab initio* chemical potentials of solid and liquid solutions and the chemistry of the Earth's core. *J. Chem. Phys.* **116,** 7127–7136 (2002).
50. Belonoshko, A., Ahuja, R. & Johansson, B. Quasi-*ab initio* molecular dynamic study of Fe melting. *Phys. Rev. Lett.* **84,** 3638–3641 (2000).
51. Laio, A., Bernard, S., Chiarotti, G., Scandolo, S. & Tosatti, E. Physics of iron at Earth's core conditions. *Science* **287,** 1027–1030 (2000).
52. Alfè, D., Gillan, M. & Price, G. Complementary approaches to the *ab initio* calculation of melting properties. *J. Chem. Phys.* **116,** 6170–6177 (2002).
53. Stacey, F. Thermodynamics of the Earth. *Rep. Prog. Phys.* **73,** 046801 (2010).
54. Ichikawa, H., Tsuchiya, T. & Tange, Y. The P–V–T equation of state and thermodynamic properties of liquid iron. *J. Geophys. Res.* **119,** 240–252 (2014).
55. Stacey, F. in *Encyclopedia of Geomagnetism and Paleomagnetism* (eds Gubbins, D. & Herrero-Bervera, E.) 91–94 (Springer, 2007).
56. Gubbins, D., Alfè, D., Masters, G., Price, G. & Gillan, M. Can the Earth's dynamo run on heat alone? *Geophys. J. Int.* **155,** 609–622 (2003).
57. Ichikawa, H. & Tsuchiya, T. Atomic transport property of Fe–O liquid alloys in the Earth's outer core P, T condition. *Phys. Earth Planet. Inter.* http://dx.doi.org/10.1016/j.pepi.2015.03.006 (2015).
58. Gubbins, D., Alfè, D., Masters, G., Price, G. & Gillan, M. Gross thermodynamics of two-component core convection. *Geophys. J. Int.* **157,** 1407–1414 (2004).
59. Davies, C. Cooling history of Earth's core with high thermal conductivity. *Phys. Earth Planet. Inter.* http://dx.doi.org/10.1016/j.pepi.2015.03.007 (2015).
60. Roberts, P. & King, E. On the genesis of the Earth's magnetism. *Rep. Prog. Phys.* **76,** 096801 (2013).
61. de Wijs, G. *et al.* The viscosity of liquid iron at the physical conditions of the Earth's core. *Nature* **392,** 805–807 (1998).
62. Lay, T., Hernlund, J. & Buffett, B. Core–mantle boundary heat flow. *Nature Geosci.* **1,** 25–32 (2009).
63. Nimmo, F. in *Treatise on Geophysics* 2nd edn, Vol. 9 (ed. Schubert, G.) 27–55 (Elsevier, 2015).
64. Jackson, A. & Livermore, P. On Ohmic heating in the Earth's core I: Nutation constraints. *Geophys. J. Int.* **177,** 367–382 (2009).
65. Roberts, P., Jones, C. & Calderwood, A. *Earth's Core and Lower Mantle* 100–129 (SEDI 2000 7th Symp., Taylor & Francis, 2003).
66. Davies, J. & Davies, D. Earth's surface heat flux. *Solid Earth* **1,** 5–24 (2010).
67. Andrault, D. *et al.* Solidus and liquidus profiles of chondritic mantle: Implication for melting of the Earth across its history. *Earth Planet. Sci. Lett.* **304,** 251–259 (2011).
68. Nakagawa, T. & Tackley, P. Influence of combined primordial layering and recycled MORB on the coupled thermal evolution of Earth's mantle and core. *Geochem. Geophys. Geosyst.* **15,** 619–633 (2014).
69. Driscoll, P. & Bercovici, D. On the thermal and magnetic histories of Earth and Venus: Influences of melting, radioactivity, and conductivity. *Phys. Earth Planet. Inter.* **236,** 36–51 (2014).
70. Labrosse, S. Thermal evolution of the core with a high thermal conductivity. *Phys. Earth Planet. Inter.* http://dx.doi.org/10.1016/j.pepi.2015.02.002 (2015).
71. Kennett, B., Engdahl, E. & Buland, R. Constraints on seismic velocities in the Earth from traveltimes. *Geophys. J. Int.* **122,** 108–124 (1995).

72. Braginsky, S. Dynamics of the stably stratified ocean at the top of the core. *Phys. Earth Planet. Int.* **111,** 21–34 (1999).
73. Loper, D. Some thermal consequences of a gravitationally powered dynamo. *J. Geophys. Res.* **831,** 5961–5970 (1978).
74. Helffrich, G. & Kaneshima, S. Causes and consequences of outer core stratification. *Phys. Earth Planet. Int.* **223,** 2–7 (2013).
75. Buffett, B. & Seagle, C. Stratification of the top of the core due to chemical interactions with the mantle. *J. Geophys. Res.* **115,** B04407 (2010).
76. Gubbins, D. & Davies, C. The stratified layer at the core–mantle boundary caused by barodiffusion of oxygen, sulphur and silicon. *Phys. Earth Planet. Inter.* **215,** 21–28 (2013).
77. Moffatt, H. & Loper, D. The magnetostrophic rise of a buoyant parcel in the Earth's core. *Geophys. J. Int.* **117,** 394–402 (1994).
78. Buffett, B. Geomagnetic fluctuations reveal stable stratification at the top of the Earth's core. *Nature* **507,** 484–487 (2014).
79. Helffrich, G. & Kaneshima, S. Outer-core compositional stratification from observed core wave speed profiles. *Nature* **468,** 807–809 (2010).
80. Gubbins, D., Alfè, D., Davies, C. & Pozzo, M. On core convection and the geodynamo: Effects of high electrical and thermal conductivity. *Phys. Earth Planet. Inter.* http://dx.doi.org/10.1016/j.pepi.2015.04.002 (2015).
81. Nakagawa, T. & Tackley, P. Lateral variations in CMB heat flux and deep mantle seismic velocity caused by a thermal-chemical-phase boundary layer in 3D spherical convection. *Earth Planet. Sci. Lett.* **271,** 348–358 (2007).
82. Olson, P. & Christensen, U. The time-averaged magnetic field in numerical dynamos with non-uniform boundary heat flow. *Geophys. J. Int.* **151,** 809–823 (2002).
83. Aubert, J., Amit, H., Hulot, G. & Olson, P. Thermochemical flows couple the Earth's inner core growth to mantle heterogeneity. *Nature* **454,** 758–761 (2008).
84. Gibbons, S. & Gubbins, D. Convection in the Earth's core driven by lateral variations in core–mantle boundary heat flux. *Geophys. J. Int.* **142,** 631–642 (2000).
85. Hollerbach, R. & Jones, C. Influence of the Earth's inner core on geomagnetic fluctuations and reversals. *Nature* **365,** 541–543 (1993).
86. Deguen, R. Structure and dynamics of Earth's inner core. *Earth Planet. Sci. Lett.* **333–334,** 211–225 (2012).
87. Labrosse, S. Thermal and compositional stratification of the inner core. *C. R. Geosci.* **346,** 119–129 (2014).
88. Lasbleis, M. & Deguen, R. Building a regime diagram for Earth's inner core. *Phys. Earth Planet. Inter.* http://dx.doi.org/10.1016/j.pepi.2015.02.001 (2015).
89. Korenaga, J. Urey ratio and the structure and evolution of Earth's mantle. *Rev. Geophys.* **46,** 2007RG000241 (2008).
90. Lythgoe, K., Rudge, J., Neufeld, J. & Deuss, A. The feasibility of thermal and compositional convection in Earth's inner core. *Geophys. J. Int.* **385,** 764–782 (2015).
91. Monnereau, M., Calvet, M., Margerin, L. & Souriau, A. Lopsided growth of Earth's inner core. *Science* **328,** 1014–1017 (2010).
92. Aubert, J., Finlay, C. & Fournier, A. Bottom-up control of geomagnetic secular variation by the Earth's inner core. *Nature* **502,** 219–223 (2013).
93. Olson, P. & Deguen, R. Eccentricity of the geomagnetic dipole caused by lopsided inner core growth. *Nature Geosci.* **5,** 565–569 (2012).
94. Nakagawa, T. & Tackley, P. Implications of high core thermal conductivity on Earth's coupled mantle and core evolution. *Geophys. Res. Lett.* **40,** 2652–2656 (2013).
95. Labrosse, S., Hernlund, J. & Coltice, N. A crystallizing dense magma ocean at the base of the Earth's mantle. *Nature* **450,** 866–869 (2007).
96. Ziegler, L. B. & Stegman, D. R. Implications of a long-lived basal magma ocean in generating Earth's ancient magnetic field. *Geochem. Geophys. Geosyst.* **14,** 4735–4742 (2013).
97. Stevenson, D. How to keep a dynamo running in spite of high thermal conductivity *AGU* (Fall Meeting 2014) abstr. #DI11C-03 (2012).
98. Amit, H. Can downwelling at the top of the Earth's core be detected in the geomagnetic secular variation? *Phys. Earth Planet. Inter.* **229,** 110–121 (2014).
99. Lesur, V., Whaler, K. & Wardinski, I. Are geomagnetic data consistent with stably stratified flow at the core–mantle boundary? *Geophys. J. Int.* **201,** 929–946 (2015).
100. Buffet, B. & Matsui, H. A power spectrum for the geomagnetic dipole moment. *Earth Planet. Sci. Lett.* **411,** 20–26 (2015).

Acknowledgements

C.D. is supported by Natural Environment Research Council (NERC) fellowships NE/H01571X/1 and NE/L011328/1 and a Green scholarship at IGPP. D.G. is supported by NSF grant EAR/1065597 and NERC grant NE/I0 12052/. M.P. is supported by NERC grants NE/H02462X/1 and NE/M000990/1. D.A. is supported by NERC grant NE/M000990/1. The authors thank T. Nakagawa, P. Driscoll, F. Nimmo and S. Labrosse for providing the model results that were used in Fig. 3.

Additional information

Supplementary information is available in the online version of the paper. Reprints and permissions information is available online at www.nature.com/reprints. Correspondence and requests for materials should be addressed to C.D.

Competing financial interests

The authors declare no competing financial interests.

Methods

Core density and composition. Seismic models of one-dimensional Earth structure provide the core density ρ, pressure P, gravity g, bulk modulus K_S, compressional velocity V_p and shear velocity V_s. V_p and V_s are very well determined, but obtaining ρ relies on the assumption that the core is close to well mixed. Model PREM (ref. 40) is often quoted as being neutrally stable (entropy and composition well mixed), yet it was derived from a neutrally stable initial model: it remains close to well mixed simply because the seismic data do not require ρ to change much. Normal modes are better at determining ρ because of their low frequency, but have poor spatial resolution because of their long wavelengths.

Model PREM has a total density jump $\Delta\rho$ at the inner core boundary (ICB) of $0.6\,\mathrm{g\,cm^{-3}}$. In this case *ab initio* densities calculated for Fe–Si–O mixtures can be compared directly to the PREM density. For our models with density jumps 0.8 and $1.0\,\mathrm{g\,cm^{-3}}$ the PREM density has to be modified, which raises the question of how much to increase the inner core density and how much to decrease the outer core density. Initially, for $0.8\,\mathrm{g\,cm^{-3}}$, we decreased the concentration in the inner core and increased the concentration of O in the outer core so the increase in the density jump was split between the two[58,101].

The $1.0\,\mathrm{g\,cm^{-3}}$ density jump was done later, by which time we decided to calculate the densities more carefully[80]. The mass of the whole core is probably the best-determined quantity to use to normalize densities, and we used the value of Masters[102]. To obtain a density profile that lay close to neutral stability we integrated the Adams–Williamson equation using seismic parameters from PREM from radius $r=0$ to the ICB, applied the required density jump, and continued integration to the core–mantle boundary (CMB). We then calculated the mass and scaled the entire density profile to give the required mass. This gave an inconsistent density profile: it used g from the original PREM model. We then recalculated g and repeated the integration and scaling. After two or three iterations this gave a self-consistent, neutrally stable density profile with the required density jump and core mass[80].

This density profile for the $1.0\,\mathrm{g\,cm^{-3}}$ jump gives the surprising result that both conductivities lie closer to the $0.6\,\mathrm{g\,cm^{-3}}$ value than the $0.8\,\mathrm{g\,cm^{-3}}$ value. This is also because of the compositions: the new density profile has a denser inner core that requires removal of a larger amount of Si from both cores and addition of correspondingly more O in the outer core. The total light element composition of the outer core, O+Si, is then closer to that for PREM than for the $0.8\,\mathrm{g\,cm^{-3}}$ jump. Furthermore, the conductivities are closer to the $0.6\,\mathrm{g\,cm^{-3}}$ values. We have not repeated the calculations for $\Delta\rho=0.8\,\mathrm{g\,cm^{-3}}$ because of the high computational cost. The PREM density changes very little by our procedure. We conclude that Si and O have a similar effect on the conductivities, which is why they change so little between $\Delta\rho=0.6\,\mathrm{g\,cm^{-3}}$ and $\Delta\rho=1.0\,\mathrm{g\,cm^{-3}}$, but this surmise has not been tested by direct calculation of different binary mixtures.

***Ab initio* calculations.** *Ab initio* simulations of core physical properties are conducted by representing a macroscopic system with a microscopic model, to be simulated on a computer. Simulations typically involve 100–1,000 atoms; the connection between the micro and macro worlds is provided by standard statistical mechanics and by thermodynamics. Electronic behaviour is described using quantum mechanics and most calculations use the implementation known as density functional theory (DFT; ref. 103). The limiting factor in modern implementations of DFT is the approximation of the exchange–correlation (XC) energy. More precise (and computationally expensive) quantum mechanics implementations are starting to emerge, for example, quantum Monte Carlo techniques[104], but there is ample accumulated evidence that DFT with standard XC functionals[105] provides very good accuracy for core materials at the relevant (P,T) conditions.

Thermodynamic properties (for example, specific heat) are usually evaluated by computing the Gibbs free energy of the system at different (P,T). This is typically done by applying standard thermodynamic integration schemes in which the Gibbs free energy is evaluated by switching the potential energy function from some chosen simple interatomic potential to the full quantum mechanical potential, and evaluating the reversible work performed in the process[106]. The statistical accuracy of the results can be controlled by the length of the simulations; the absolute accuracy depends on the quality of the quantum mechanics description. Quantities such as the electrical conductivity and the electronic component of the thermal conductivity are also evaluated by sampling the relevant high-(P,T) systems, and in the DFT formulation are computed by using the Kubo–Greenwood (KG) formulation[107,108], which essentially involves the evaluation of matrix elements of the electron momentum operator. Specifically, the formula for the electrical conductivity as a function of frequency ω for a particular $\mathbf{k}$-point in the Brillouin zone of the simulation supercell and for a particular configuration of the ions $\{R_I\}$ reads

$$\sigma_k(\omega;R_I)=\frac{2\pi e^2\hbar^2}{3m^2\omega\Omega}\sum_{i,j=1}^{n}\sum_{\alpha=1}^{3}[F(\epsilon_{i,\mathbf{k}})-F(\epsilon_{j,\mathbf{k}})]|\langle\Psi_{j,\mathbf{k}}|\nabla_\alpha|\Psi_{i,\mathbf{k}}\rangle|^2 \times\delta(\epsilon_{j,\mathbf{k}}-\epsilon_{i,\mathbf{k}}-\hbar\omega)$$

where e and m are the electron charge and mass respectively, $\hbar$ is Planck's constant divided by 2π, Ω is the volume of the simulation cell and n the number of Kohn–Sham states. The α sum runs over the three spatial directions, which in a liquid are all equivalent. $\Psi_{i,\mathbf{k}}$ is the Kohn–Sham wavefunction corresponding to eigenvalue $\epsilon_{i,\mathbf{k}}$ and $F(\epsilon_{i,\mathbf{k}})$ is the Fermi weight. The d.c. conductivity σ_0 is given by the value of $\sigma(\omega)$ in the limit $\omega\to0$. The Kohn–Sham states represent independent particles in DFT, interacting among themselves through an effective mean field. Because of this the DFT-KG expression does not include interactions between these particles, and it therefore is often regarded as not including electron–electron interactions, although formally there is no mapping between the KS states and the real electrons in the system.

In a free-electron liquid the electronic part of the thermal conductivity κ_0 and the electrical conductivity σ_0 are related by the Wiedemann–Franz (WF) law, $L=\kappa_0/(\sigma_0T)$, where L is the Lorenz number, equal to $2.44\times10^{-8}\,\Omega\,\mathrm{W\,K^{-2}}$ in the ideal case. Because the ionic component of the thermal conductivity is a small fraction of the total (a few %) it is usually neglected, and often the thermal conductivity is simply obtained from the electrical conductivity using the WF law and the ideal value of the Lorenz number. However, in a real system there is no reason why the WF law should be satisfied, and in fact deviations are observed for several metals at ambient conditions.

The electronic component of the thermal conductivity can be directly calculated using the Chester–Thellung[109] formulation of the Kubo–Greenwood formula, which reads

$$\kappa(\omega)=\frac{1}{e^2T}\left(L_{22}(\omega)-\frac{L_{12}(\omega)^2}{\sigma(\omega)}\right)$$

and κ_0 is the value of $\kappa(\omega)$ in the limit $\omega\to0$. The kinetic coefficients $L_{lm}(\omega)$ are given by[110]:

$$L_{lm}(\omega)=(-1)^{(l+m)}\frac{2\pi e^2\hbar^2}{3m^2\omega\Omega}\sum_{i,j=1}^{n}\sum_{\alpha=1}^{3}[F(\epsilon_{i,\mathbf{k}})-F(\epsilon_{j,\mathbf{k}})]|\langle\Psi_{j,\mathbf{k}}|\nabla_\alpha|\Psi_{i,\mathbf{k}}\rangle|^2 \times[\epsilon_{j,\mathbf{k}}-\mu]^{(l-1)}[\epsilon_{i,\mathbf{k}}-\mu]^{(m-1)}\delta(\epsilon_{j,\mathbf{k}}-\epsilon_{i,\mathbf{k}}-\hbar\omega)$$

where μ is the chemical potential. Standard DFT calculations[24] find that the WF law is indeed followed very well by pure iron at Earth's core conditions, with only slight deviations for iron–silicon–oxygen mixtures[25].

Core energetics model. The governing equations describing global energy and entropy balance have been described in detail elsewhere[56,58,63]. Various forms have been used in the literature[58,70,111], but all are equivalent[112]. Averaging over a timescale that is long compared to the timescale associated with fluctuations of the dynamo process but short compared to the evolutionary timescale of the core it is assumed that convection mixes the outer core to a basic state of hydrostatic equilibrium, uniform composition ($\nabla c_X^L=0$, where c_X^L is the mass concentration of light impurity X in the liquid), and an adiabatic temperature $T_a(r)$. Radial variations in thermodynamic properties are supposed to far exceed lateral variations[113], and so all variables are assumed to vary only in radius r with r_o the CMB and $r_i(t)$ the ICB, which changes in time t as the inner core grows. These approximations are also taken to hold in the inner core. Because the core is assumed adiabatic and well mixed the temperature at any depth is simply related to that at the CMB (ref. 63). With these approximations, the energy balance can be written as[56,58]

$$\underbrace{-\oint k\nabla T\cdot\mathbf{n}\,\mathrm{d}S}_{Q_{\mathrm{cmb}}}=\underbrace{-\frac{C_P}{T_o}\int\rho T_a\mathrm{d}V\frac{\mathrm{d}T_o}{\mathrm{d}t}}_{Q_S}\underbrace{-4\pi r_i^2L\rho_iC_r\frac{\mathrm{d}T_o}{\mathrm{d}t}}_{Q_L} +\underbrace{\alpha_c\frac{\mathrm{D}c_X^L}{\mathrm{D}t}\int\rho\psi\mathrm{d}V}_{Q_g}+\underbrace{\int\rho h\mathrm{d}V}_{Q_r} \quad (3)$$

where $\psi(r)$ is the gravitational potential,

$$\frac{\mathrm{D}c_X^L}{\mathrm{D}t}=\frac{4\pi r_i^2\rho_i}{M_{oc}}C_r(c_X^L-c_X^S)\frac{\mathrm{d}T_o}{\mathrm{d}t} \quad (4)$$

and

$$C_r=\frac{1}{\left(\frac{\mathrm{d}T_m}{\mathrm{d}P}\right)_{r=r_i}-\left(\frac{\partial T_a}{\partial P}\right)_{r=r_i}}\frac{1}{\rho_ig_i}\frac{T_i}{T_o}$$

Quantities are defined in Table 1 of the main text. Subscripts i and o denote quantities evaluated at the ICB and CMB respectively. In writing equation (3) the CMB has been assumed to be insulating and C_P, α_c and L have been assumed constant. Small terms associated with core contraction have been omitted[56]. In writing equation (4) it has been assumed that the concentration of element X in the solid, c_X^S, does not vary in time, which is a good approximation[59,70]. Note that Q_{cmb}

is the total CMB heat flux that is set by mantle convection and not the adiabatic heat flux. **n** is the outward normal to the surface S, which encloses the volume V of the core.

Equation (3) states that the total CMB heat flow Q_{cmb} is balanced by heat released from cooling the core Q_S, latent heat release due to the phase change at the ICB Q_L, gravitational energy due to the segregation of light elements into the liquid phase on freezing Q_g, and radiogenic heating Q_r. It describes the thermal evolution of the core but does not explicitly contain the magnetic field and hence does not say anything about maintaining the geodynamo. The magnetic field **B** does appear in the entropy balance, which can be written[56,58]

$$\underbrace{\frac{1}{\mu_0^2}\int\frac{(\nabla\times\mathbf{B})^2}{T_{\mathrm{a}}\sigma}\mathrm{d}V}_{E_{\mathrm{J}}}+\underbrace{\int k\left(\frac{\nabla T_{\mathrm{a}}}{T_{\mathrm{a}}}\right)^2\mathrm{d}V}_{E_{\mathrm{k}}}+\underbrace{\alpha_c^2\alpha_X^D\int\frac{g^2}{T_{\mathrm{a}}}\mathrm{d}V}_{E_{\mathrm{a}}}$$

$$=\underbrace{\int\rho C_P\frac{T_{\mathrm{a}}}{T_o}\left(\frac{1}{T_{\mathrm{a}}}-\frac{1}{T_o}\right)\mathrm{d}V\frac{\mathrm{d}T_o}{\mathrm{d}t}}_{E_S}\underbrace{-Q_L\frac{(T_i-T_o)}{T_iT_o}}_{E_L}$$

$$+\underbrace{\frac{Q_g}{T_o}}_{E_{\mathrm{g}}}+\underbrace{\int\rho h\left(\frac{1}{T_{\mathrm{a}}}-\frac{1}{T_o}\right)\mathrm{d}V}_{E_r}\tag{5}$$

This equation shows that three positive definite sources of entropy, the dynamo entropy E_{J}, entropy of thermal conduction E_{k}, and the entropy of molecular diffusion of light elements (barodiffusion) E_{a}, balance entropy production associated with secular cooling E_S, gravitational energy release E_{g}, latent heat release E_{L} and radiogenic heating E_r. The heat of reaction is small and has been neglected in (5); the viscous dissipation, which is supposed to be small in the core[56], has also been neglected. Note that the thermodynamic efficiency of the E_{g} term is greater than the other terms because it contains the factor $(1/T_o)$ rather than the smaller factor $(1/T_{\mathrm{a}}-1/T_o)$.

Equations (3) and (neqrefeq7) can be written in the compact form[9,58]

$$Q_{\mathrm{cmb}}=(\tilde{Q}_S+\tilde{Q}_L+\tilde{Q}_g)\frac{\mathrm{d}T_o}{\mathrm{d}t}+Q_r\tag{6}$$

$$E_{\mathrm{J}}+E_{\mathrm{k}}+E_{\mathrm{a}}=(\tilde{E}_S+\tilde{E}_L+\tilde{E}_g)\frac{\mathrm{d}T_o}{\mathrm{d}t}+E_r\tag{7}$$

where $Q_L=(\tilde{Q}_L\mathrm{d}T_o)/\mathrm{d}t$ and similarly for other terms. The tilde quantities can be calculated using estimates of core material properties. Equations (6) and (7) show that knowledge of the CMB heat flux Q_{cmb} and the amount of radiogenic heat production per unit mass h determines the cooling rate of the core $\mathrm{d}T_o/\mathrm{d}t$, and hence the dynamo entropy E_{J}. $\mathrm{d}T_o/\mathrm{d}t$ is also related to the growth rate of the inner core, $\mathrm{d}r_i/\mathrm{d}t$, by[56]

$$\frac{\mathrm{d}r_i}{\mathrm{d}t}=C_r\frac{\mathrm{d}T_o}{\mathrm{d}t}$$

Equations (6) and (7) are solved by the method described in ref. 59. Unlike this previous study we do not include S; the differences are minor because the partitioning behaviours of S and Si are very similar. Both O and Si contribute to the gravitational energy, although the latter is a very small effect. The effect of the density jump on g is very small and can safely be ignored; the jump in k at the ICB is also ignored.

References

101. Alfè, D., Gillan, M. & Price, G. Composition and temperature of the Earth's core constrained by combining *ab initio* calculations and seismic data. *Earth Planet. Sci. Lett.* **195,** 91–98 (2002).
102. Masters, T. in *Encyclopedia of Geomagnetism and Paleomagnetism* (eds Gubbins, D. & Herrero-Bervera, E.) 82–85 (Springer, 2007).
103. Parr, R. & Yang, W. *Density-Functional Theory of Atoms and Molecules* (Oxford Univ. Press, 1989).
104. Foulkes, W., Mitáš, L., Needs, R. & Rajagopal, G. Quantum Monte Carlo simulations of solids. *Rev. Mod. Phys.* **73,** 33–83 (2001).
105. Wang, Y. & Perdew, J. Correlation hole of the spin-polarized electron gas, with exact smallwave-vector and high-density scaling. *Phys. Rev. B* **44,** 13298 (1991).
106. Frenkel, D. & Smit, B. *Understanding Molecular Simulation* (Academic, 1996).
107. Kubo, R. Statistical-mechanical theory of irreversible processes. I. General theory and simple applications to magnetic and conduction problems. *J. Phys. Soc. Jpn* **12,** 570–586 (1957).
108. Greenwood, D. The Boltzmann equation in the theory of electrical conduction in metals. *Proc. Phys. Soc.* **71,** 585–596 (1958).
109. Chester, G. & Thellung, A. The law of Wiedemann and Franz. *Proc. Phys. Soc.* **77,** 1005–1013 (1961).
110. Mazevet, S., Torrent, M., Recoules, V. & Jollet, F. Calculations of the transport properties within the PAW formalism. *High Energ. Dens. Phys.* **6,** 84–88 (2010).
111. Buffett, B., Huppert, H., Lister, J. & Woods, A. On the thermal evolution of the Earth's core. *J. Geophys. Res.* **101,** 7989–8006 (1996).
112. Lister, J. Expressions for the dissipation driven by convection in the Earth's core. *Phys. Earth Planet. Inter.* **140,** 145–158 (2003).
113. Stevenson, D. Limits on lateral density and velocity variations in the Earth's outer core. *Geophys. J. Int.* **88,** 311–319 (1987).